

Dartmouth College

Dartmouth Digital Commons

Dartmouth Scholarship

Faculty Work

2021

Examining the Auroral Ionosphere in Three Dimensions Using Reconstructed 2D Maps of Auroral Data to Drive the 3D GEMINI Model

Robert Clayton

Embry-Riddle Aeronautical University

Meghan Burleigh

Naval Research Laboratory

Kristina A. Lynch

Dartmouth College, Kristina.A.Lynch@dartmouth.edu

Matt Zettergren


Embry-Riddle Aeronautical University

Tucker Evans

Dartmouth College; Massachusetts Institute of Technology

Follow this and additional works at: <https://digitalcommons.dartmouth.edu/facoa>

See next page for additional authors

 Part of the [Physical Sciences and Mathematics Commons](#)

Dartmouth Digital Commons Citation

Clayton, Robert; Burleigh, Meghan; Lynch, Kristina A.; Zettergren, Matt; Evans, Tucker; Grubbs, Guy; Hampton, Donald L.; Hysell, David; Kaeppler, Stephen; Lessard, Marc; Mitchell, Robert; Reimer, Ashton; Roberts, T. Maximillian; Samara, Marilia; and Varney, Roger, "Examining the Auroral Ionosphere in Three Dimensions Using Reconstructed 2D Maps of Auroral Data to Drive the 3D GEMINI Model" (2021). *Dartmouth Scholarship*. 4299.

<https://digitalcommons.dartmouth.edu/facoa/4299>

This Article is brought to you for free and open access by the Faculty Work at Dartmouth Digital Commons. It has been accepted for inclusion in Dartmouth Scholarship by an authorized administrator of Dartmouth Digital Commons. For more information, please contact dartmouthdigitalcommons@groups.dartmouth.edu.

Authors

Robert Clayton, Meghan Burleigh, Kristina A. Lynch, Matt Zettergren, Tucker Evans, Guy Grubbs, Donald L. Hampton, David Hysell, Stephen Kaeppler, Marc Lessard, Robert Mitchell, Ashton Reimer, T. Maximillian Roberts, Marilia Samara, and Roger Varney

JGR Space Physics

RESEARCH ARTICLE

10.1029/2021JA029749

Key Points:

- Three-dimensional physics-based Geospace Environment Model of Ion-Neutral Interactions (GEMINI) ionospheric model driven with two-dimensional reconstructions of auroral data for non-idealized view of auroral current closure
- Conductance gradients are shown to be significant for current closure in these examples, including Hall conductance gradients in some cases
- Exploration of sensitivity of GEMINI output to fidelity of data reconstruction input drivers at radar and in situ resolutions

Supporting Information:

Supporting Information may be found in the online version of this article.

Correspondence to:













K. A. Lynch,
kal@dartmouth.edu

Citation:

Clayton, R., Burleigh, M., Lynch, K. A., Zettergren, M., Evans, T., Grubbs, G., et al. (2021). Examining the auroral ionosphere in three dimensions using reconstructed 2D maps of auroral data to drive the 3D GEMINI model. *Journal of Geophysical Research: Space Physics*, 126, e2021JA029749. <https://doi.org/10.1029/2021JA029749>

Received 2 JUL 2021
Accepted 12 OCT 2021

Examining the Auroral Ionosphere in Three Dimensions Using Reconstructed 2D Maps of Auroral Data to Drive the 3D GEMINI Model

Robert Clayton¹ , Meghan Burleigh² , Kristina A. Lynch³ , Matt Zettergren¹ , Tucker Evans^{3,4}, Guy Grubbs⁵ , Donald L. Hampton⁶ , David Hysell⁷ , Stephen Kaeppler⁸ , Marc Lessard⁹ , Robert Michell¹⁰, Ashton Reimer¹¹ , T. Maximillian Roberts¹², Marilia Samara¹³ , and Roger Varney¹¹ 

¹Embry-Riddle Aeronautical University, Daytona Beach, FL, USA, ²Naval Research Laboratory, Washington, DC, USA, ³Dartmouth College, Hanover, NH, USA, ⁴Massachusetts Institute of Technology, Boston, MA, USA, ⁵Southwest Research Institute, San Antonio, TX, USA, ⁶University of Alaska Fairbanks, Fairbanks, AK, USA, ⁷Cornell University, Ithaca, NY, USA, ⁸Clemson University, Clemson, SC, USA, ⁹University of New Hampshire, Durham, NH, USA, ¹⁰University of Maryland, College Park, MA, USA, ¹¹SRI International, Menlo Park, CA, USA, ¹²NASA Jet Propulsion Laboratory, Pasadena, CA, USA, ¹³NASA Goddard Space Flight Center, Greenbelt, MD, USA

Abstract We use the Geospace Environment Model of Ion-Neutral Interactions (GEMINI) to create three-dimensional, time-dependent simulations of auroral ionospheric parameters in the localized, several 100 km region surrounding auroral arcs observed during a winter 2017 sounding rocket campaign, resolving three-dimensional features of fine-scale (km) flow structures in the vicinity of an auroral arc. The three-dimensional calculations of GEMINI allow (with sufficient driving data) auroral current closure to be investigated without idealizing assumptions of sheet-like structures or height integrated ionospheres. Datamaps for two nearly sheet-like arcs are reconstructed from replications of the Isinglass sounding rocket campaign data, and combined with camera-based particle inversions into a set of driving inputs to run the 3D time-dependent model. Comparisons of model results to radar density profiles and to in situ magnetometry observations are presented. Slices of volumetric current, flow, and conductance structures from model outputs are used to interpret closure currents in an auroral arc region, and are compared to original in situ measurements for verification. The predominant source of return current region field aligned current closure for these slow time variation events is seen to be from the conductance gradients, including the Hall. The importance of the $\nabla \Sigma_H$ versus $\nabla \Sigma_P$ terms in the determination of the current structure provides a more complicated picture than a previous GEMINI study, which relied predominantly on the divergence of the electric field to determine current structure. Sensitivity of data-driven model results to details of replication and reconstruction processes are discussed, with improvements outlined for future work.

1. Introduction

In this study, we present case study examples from the March 2017 Isinglass auroral sounding rocket campaign interpreted through the Geospace Environment Model of Ion-Neutral Interactions (GEMINI) ionospheric model, focusing on modeled current structures and their interpretation through current closure equations. We generate a 3D and time-dependent localized simulation of auroral ionospheric parameters in the region surrounding a night-side discrete auroral arc, with sufficiently small scale to reproduce the features near an auroral arc boundary, in order to resolve and interpret flow structures, currents, and plasma responses in the vicinity of an auroral arc. The expectations of the auroral environment near stable arc structures are outlined by G. Marklund et al. (1982). Marghitsu (2012) has further discussed the implications for spatially variable conductance and electric fields and has related these to various stages of the substorm cycle. Following current continuity in the ionospheric system, the (non-inductive) field aligned component of the current can be described as in Brekke et al. (1989) and more generally using Marghitsu (2012), in a height-integrated viewpoint, as:

$$j_z = (\nabla \cdot \mathbf{E}) \Sigma_p + \nabla \Sigma_p \cdot \mathbf{E} - \nabla \Sigma_H \cdot (\hat{\mathbf{e}}_1 \times \mathbf{E}) \quad (1)$$

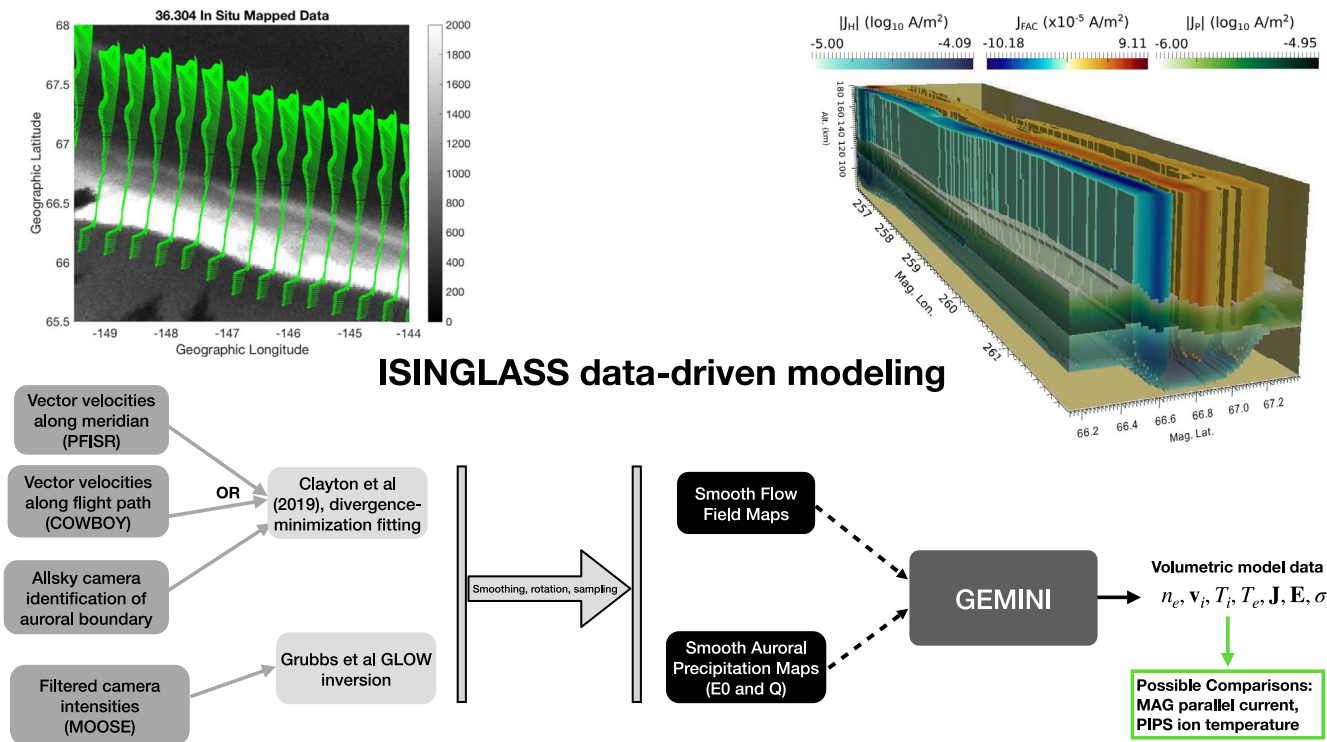


Figure 1. (Top left) Example of data replication technique described in Clayton et al. (2019); 2D map of flow data created by replicating the in situ data from along the rocket trajectory, at many places along the observed visible arc boundary. (Bottom) Flowchart of the data-driving process of the 3D Geospace Environment Model of Ion-Neutral Interactions model, from input data fields to volumetric output for electron density, ion velocity, ion and electron temperature, 3D current, 3D electric field, and conductivities. (Top right) Model output for one example case (c5 at 7:52:45 UT) of the Isinglass event: a three-dimensional representation of the volume currents in the model space, including the field-aligned currents (return current in blue and precipitating-electron current in orange), Hall (light blue), and Pedersen (green). Note that the sign conventions and colors here deviate from other figures.

Here j_z is the field-aligned current, \mathbf{E} is the ionospheric electric field, $\hat{\mathbf{e}}_1$ is a unit vector along the geomagnetic field, and Σ_p, Σ_H are the Pedersen and Hall conductances (height integrated conductivity), respectively. Throughout this manuscript, we use a formal sign convention for field-aligned current whereby in the Northern hemisphere, electrons precipitating downward toward the atmosphere, carrying negative charge parallel to the Earth \mathbf{B} , are considered a negative field-aligned current; return currents (i.e., upgoing electrons) are considered a positive field-aligned current. Equation 1 expectations for current continuity are explored, for examples, where the auroral structures are stable and relatively invariant in the longitudinal (along-arc) direction and in time. We begin to account for small variations in the along-arc direction using the arc boundary information from auroral imagery (Clayton et al., 2019), but further information is needed for more complex arc structures. Accounting for the non-idealized, non-sheetlike features of the arc allows progress in our understanding of the accurate determination of the 3D auroral environment (Hwang et al., 2006). For the examples presented here, only variations of the arc boundary are considered. Future campaigns with multi-point sensing can take more complex arc structures into account. Equation 1 shows a height-integrated expectation. GEMINI (M. Zettergren & Semeter, 2012; M. D. Zettergren & Snively, 2019) allows us to investigate this system in three-dimensions. Data-driven modeling at mesoscales (not resolved in global simulations) is challenging given the local nature of the model and the need to properly include boundary and initial conditions (hysteresis and forcing).

For the purposes of driving a model and solving the non-height-integrated version of Equation 1, complete uniformly gridded 2D maps (F-region, perpendicular to the magnetic field) of vector $\mathbf{E} \times \mathbf{B}$ flow field data and particle precipitation data are desired (see Figure 1). This complete map of data across the top of the model space is achieved by a data synthesis process (Clayton et al., 2019) using plasma flow taken from a 1D line of ground-based or in situ measurements along a cross-arc cut (i.e., along a rocket trajectory, or along the central axis of the Poker Flat Incoherent Scatter Radar [PFISR] field of view), and particle

precipitation measurements from ground-based filtered multispectral imagers (Grubbs, Michell, Samara, Hampton, Hecht, et al., 2018; Grubbs, Michell, Samara, Hampton, & Jahn, 2018). Our field of interest is a several 100 km region in central Alaska, encompassing the PFISR radar field of view and the trajectory of the 36.304 Isinglass rocket launched from Poker Flat.

In this study, using 2D maps of reconstructed flow data, together with inverted filtered imagery, to drive the 3D GEMINI model, we calculate the 3D auroral environment near stable arc structures. An example volumetric current system output is illustrated in Figure 1, top right. We discuss what can be seen from a three-dimensional as opposed to an idealized-sheet-like, height-integrated auroral morphology interpretation. Our study comprises two comparisons. We investigate, in Comparison One, the relative significance of different contributors to current closure (including along-arc variations and non-height-integrated effects) in a 3D volume as seen in two different auroral events. In Comparison Two, we show the sensitivity of the simulation output to the effects of driver-data scale size. Specifically, we study the model-calculated current structures in one auroral event using different driving input flow field data sets (PFISR vs. in situ based flow data, with different reconstruction techniques) at different data resolutions.

In Section 2, we provide a brief summary of the GEMINI ionospheric model, and a description of how the data inputs are prepared for use in driving the model. In Section 3, we present the specific data inputs to be used to drive the model for four cases, including how they are generated from the raw data in the Isinglass campaign: camera imagery, PFISR radar data, and in situ measurements. In Sections 4 and 5, we analyze the output of the GEMINI model for the four cases, specifically the current and conductance maps over the region of interest for the different events and the different data sets we consider.

2. Methodology

The example flow field shown in Figure 1 provides a map of 2D F-region vector flow velocity (equivalent, as \mathbf{ExB}/B^2 , to the information of the DC electric field). The visible arc signatures provide a 2D map of precipitation. The combination can be used to constrain a calculation of the 3D volumetric region near the arc. The electric field can be mapped along field lines (assuming equipotential field lines through the E and F regions), but the flow field is altitude-dependent, and a slice at one altitude does not contain the entire 3D picture. Correctly defining the plasma motions and densities in the auroral volume requires calculation of plasma transport. To calculate the ionospheric environment, we use the GEMINI 3D model (M. D. Zettergren & Snively, 2019). Inputs for the model are constrained using data as illustrated in the flowchart representation in Figure 1. Driving data sets consist of particle data generated from ground-based multispectral camera inversions, and electric field data (flow field data) generated from in situ measurements or from ground-based radars. Detailed descriptions of GEMINI (M. D. Zettergren & Snively, 2015) and online documentation information (M. D. Zettergren et al., 2015) are available.

The GEMINI code is open source and links to the documentation and source code repository for the model can be found in the Acknowledgments section. The GEMINI 3D model is built on the previous 2D version of GEMINI (M. Zettergren & Semeter, 2012), which solves a multi-fluid system of equations in general orthogonal curvilinear coordinates describing ionospheric plasma dynamics coupled to a module describing self-consistent ionospheric electrodynamics. The fluid system of equations conserves mass, momentum, and energy for each ionospheric species relevant to the E, F, and topside regions. In this study, input electric fields are used to compute perpendicular current density via Ohm's law which can then be used to derive parallel current density by enforcing $\nabla \cdot \mathbf{J} = 0$ (assuming the field lines are equipotentials). Driving input data maps of (a) particle precipitation energy flux and (b) average energy, and (c) DC electric fields (vector \mathbf{ExB}/B^2 flow fields) are imposed on the top of the model domain using the data generated during the Isinglass campaign. GEMINI then solves the 3D model domain for the self-consistent auroral ionosphere, including volumetric current density. Throughout this manuscript, neutral wind effects are neglected as small, and both \mathbf{E} and \mathbf{ExB}/B^2 flow are quantities in the frame of reference of the ground. We also neglect diamagnetic, inertial, and gravitational drifts and current for this study; an appropriate assumption for the scales and locations of interest here. It is noted that, this is the first application of GEMINI to use 2D mapped data products to specify boundary conditions for 3D auroral simulations—a new GEMINI capability built for this study.

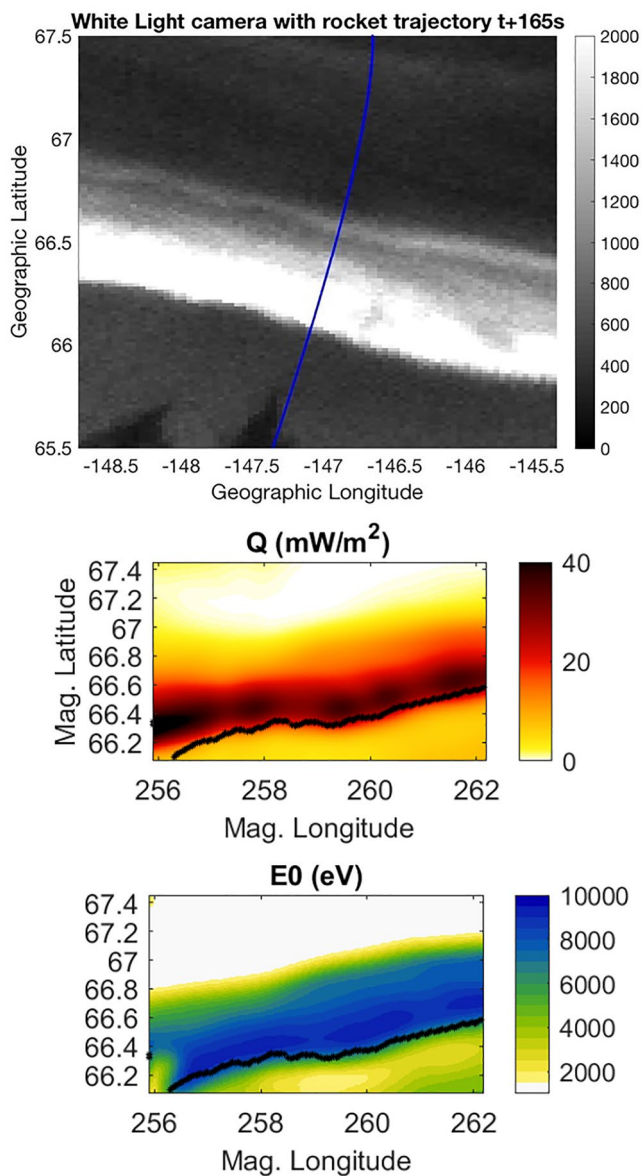


Figure 2. Summary of process of ground based camera (top, geographic coordinates) to model input (center, bottom, and geomagnetic coordinates), via filtered camera inversion. The output of multi-spectral camera inversions provides maps of energy flux (center) and average energy (bottom) of precipitating particles over the model field of view where auroral emissions are present. Where the precipitating energy flux is too low for a viable inversion, a data floor is applied. The top panel shows a higher resolution white light image used for arc boundary definition.

An example three-dimensional output representation of volume currents for the Isinglass event is shown in Figure 1. For these particular event studies, we have chosen a rectangular model grid in geomagnetic coordinates with non-uniform spacing in altitude. The Cartesian model grid is 128×128 cells in the latitude/longitude plane, covering approximately 2° in latitude and 6° in longitude with pixel spacing of 1 km in latitude and 2 km in longitude. The altitude dimension (taken to be magnetic-field-aligned) is 168 cells distributed non-uniformly covering 80–1,000 km altitude.

Initial conditions for the GEMINI simulations are adjusted so that the F-region density in the model is similar to the averages seen over the PFISR field-of-view. Initial conditions to GEMINI can be specified arbitrarily; in our case we run a simulation to near equilibrium from some presumed ionospheric state and take this simulation output as our initial conditions. By adjusting the input to this “equilibrium” simulation one can roughly match F-region density from radar data while maintaining an approximate equilibrium (by allowing the simulation to run for many hours so that transients from the initial presumption settle).

Camera inversions from multispectral filtered imagery (Grubbs, Michell, Samara, Hampton, Hecht, et al., 2018; Grubbs, Michell, Samara, Hampton, & Jahn, 2018) provide maps of average energy and energy flux of precipitating particles over the model grid-space. As illustrated in Figure 2, maps of these energy and flux inversion results are interpolated to the model grid space in geomagnetic latitude and longitude. The inversion products are floored to a threshold energy flux value of 0.025 mW/m^2 , in order to ignore bad inversions from regions of minimal or no precipitation. Additionally, the calculated average energy is floored to a value of 1 keV; below this value, the inversions are not reliable enough to be used quantitatively for this study.

Electric field data maps to drive the model are generated from ground-based or in situ DC plasma flow measurements, replicated along stable arc boundaries to fill the latitude/longitude grid space of the model (Clayton et al., 2019). This data replication process assumes that the arc structure being measured is relatively longitudinally invariant and time stable over the span in space and time of the model simulation. For the events selected here, these assumptions are observed to be true from the filtered imagery inversions. Clayton et al. (2019) details the process, summarized below, of *replicating* the measured plasma flow data along the arc, and then interpolating to the model grid with a minimal-divergence constraint—the *reconstruction*. We note to the reader that we use the term “replication” specifically to mean moving from a 1D line of measured flow vectors, to an irregularly gridded 2D field of flow vectors; and the term “reconstruction” to mean the divergence-minimized, interpolated-to-regular-lattice field. Example results of this process, shown as an HSV (Hue-Saturation-Value) representation of the F-region flow field, for our four case study events (c1, c3, c5, and c6; defined in Table 1) are shown in Figure 3. The HSV representation uses color to indicate the geomagnetic direction of the vector data and color saturation corresponds to strength, saturated at a value of 600 m/s. The c1, c3, and c5 reconstructions use the reconstruction process detailed in Clayton et al. (2019); the c6 methodology is additionally processed.

Reconstructing the replicated flow field data into a 2D field suitable for driving the 3D time-dependent GEMINI model takes some care. The model grid is different from the irregular array of locations on which the measurement data are replicated, and a method to interpolate the 2D maps of flow field data onto the

Table 1
Geospace Environment Model of Ion-Neutral Interactions Driving Field Data Sets

Data set	Description	Fit
c1	Imagery and PFISR flow, “0704”: 070100–070950 UT	Constrained vector fit
c3	Imagery and PFISR flow, “0753” 075240–075510 UT	Constrained vector fit
c5	Imagery and in situ flow, “0753” 075240–075455 UT	Constrained vector fit
c6	Imagery and c5 flow, “0753” 075240–075400 UT	Arc-aligned scalar fit

model grid is needed in order to generate the reconstructions shown in Figure 3. A simple interpolation to a regular grid (and indeed, the simple replication process itself) introduces spurious divergences in the flow (or, curls in the electric field). We use two different reconstruction processes here. For both, in the upper F-region with an electrostatic assumption (i.e., electric field derivable from a scalar potential field), the plasma flow field is considered divergence-free (for a locally uniform magnetic field) and the electric field is curl-free.

In the first process, therefore, we interpolate the (replicated, irregular) plasma flow vector field data to the model grid through a minimization process which constrains the divergence of the resulting interpolated vector field (Dartmouth Senior Honors Thesis, Tucker Evans, 2019; summarized in Appendix of Clayton et al., 2019). Since the replications are very dense, the divergence-minimization constraint pushes the solution to one close to the replication field, without extraneous eddies. Furthermore, the data are smoothed as they are interpolated, to remove spikes in the data and its derivatives that cause non-physical results in the model. Simple linear or cubic interpolations do not satisfy the divergence-minimization constraints. The

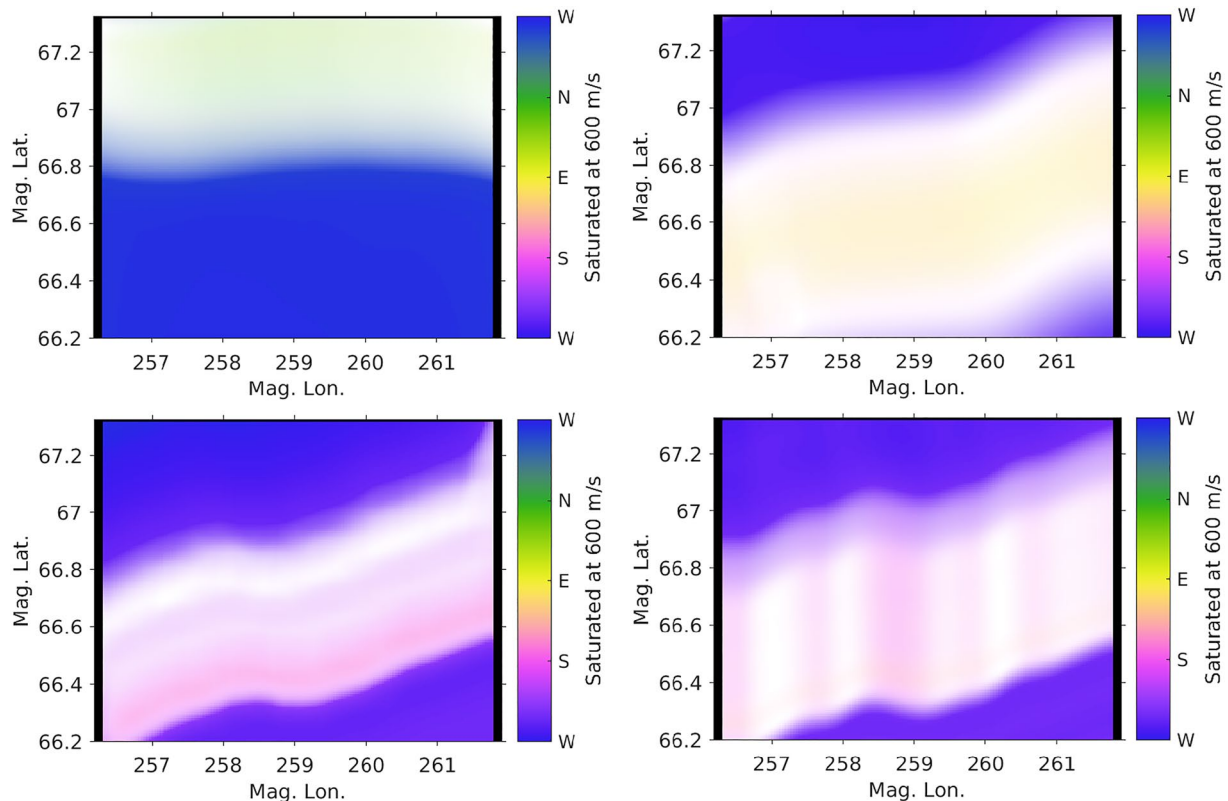


Figure 3. 2D flow field reconstructed data maps for model driving of case study events c1 (top left), c3 (top right), c5 (lower left), and c6 (lower right). See Table 1 for case event descriptions. Timeframes shown are 07:04:00 UT for c1, and 07:52:45 UT for the others. The Hue-Saturation-Value representation used here has color indicating the geomagnetic direction of the vector data, and brightness corresponding to strength, saturated at a value of 600 m/s.

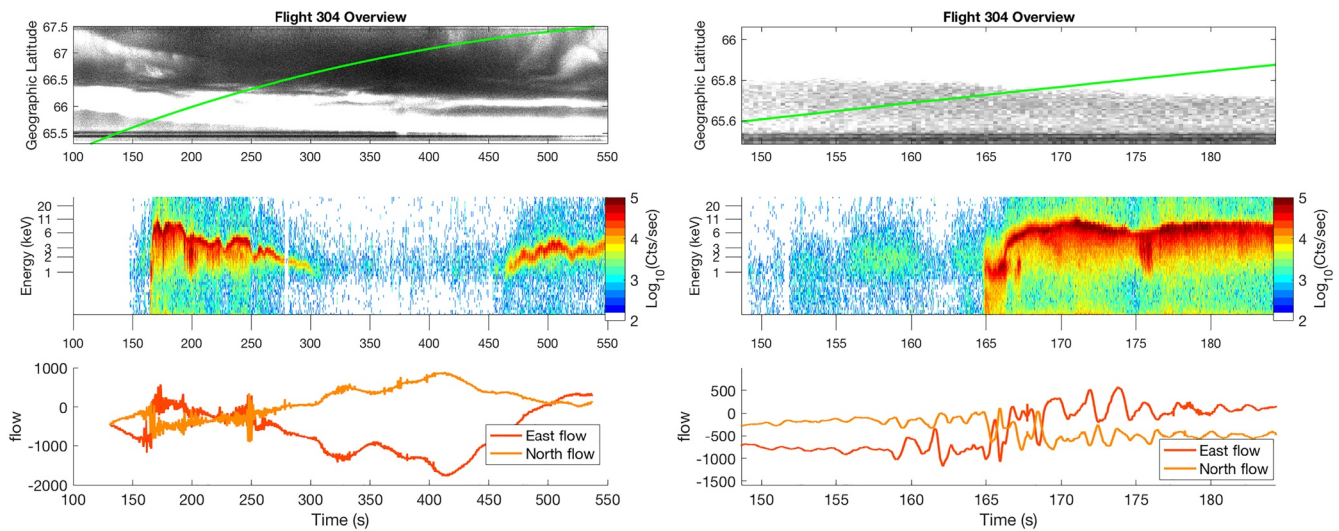


Figure 4. Originating data for c3, c5, and c6 reconstructions. Top: keogram from white light imager. Center: in situ electron precipitation observations. Bottom: in situ flow vector data at kHz sampling with relative attitude deconvolution. Right panels: zoom at arc entry point near 075245 UT = T+165 s flight time.

minimization algorithm is used to optimally fit the vector field data to the lattice, constrained with minimal divergence. We refer to this reconstruction process as a “constrained vector fit.”

The second procedure for reconstructing the flow field from the replicated data is as follows. This process grows from ideas presented in Nicolls et al. (2014) and Donoho and Duncan (2000); it uses an explicit incorporation of information from accompanying auroral imagery. For this process, the reconstruction algorithm is based on two assumptions: that the resultant field should be divergence free, and also that it should be nearly invariant along the direction of the arc boundary. The boundary can be extracted from corresponding imagery, or if that is not available, from density information or direct analysis of minimum variance directions in the flow and magnetometry data. As detailed in the Appendix A, a scalar basis function representation for the electrostatic potential field is found which gives a flow field consistent with these two assumptions, and with the available data. The resolution of the reconstruction can be no better than twice the width of the underlying basis functions, indicating that in the case used here the resolution should be approximately 0.15° of magnetic latitude, on the order of 10–20 km. Denser data along the axis perpendicular to the arc will allow higher resolution reconstructions. We refer to this reconstruction process as “arc-aligned scalar fit.”

For either flow reconstruction technique, either the constrained vector fit or the arc-aligned scalar potential fit, the resulting regularly gridded flow maps are then converted to electric field, taking $\mathbf{E} = -\mathbf{v} \times \mathbf{B}$ in the F-region ionosphere, and used as input at the top boundary of the model. Examples of the constrained vector fit are shown in Figure 3 as c1, c3, and c5 (runs are specified in Table 1); and of the arc-aligned scalar fit in the same figure, as c6. Differences between c5 and c6 are apparent; in particular, the c6 version takes variations in the direction of the arc boundary angle into account in the 2D field.

The scale size of features, we expect to be able to reconstruct using this model is a function both of the scale size of the input data, and of the processing required to distribute the driving data over the model grid. In Comparison Two below we compare PFISR-radar-driven event studies to in situ-flow-driven event studies. It is important to remember that the originating flow data are along one-dimensional cross-arc cuts. Figure 4 shows the in situ flow data (at its highest cadence) together with a keogram of the white light imagery and a spectrogram of the in situ particle data. The in situ flow data are shown here at the original kHz sampling rate with a relative attitude deconvolution (only relatively, not absolutely, fit to a North/East local reference frame). The sharpness of the arc boundary is evident in the particle data, and the flow vector is fixed, other than Alfvénic variations, for 0.25° of latitude equatorward of the boundary. Later, we will see that processing of the 2D flow field reconstruction smooths this sharp change in the flow vector such that it appears to change equatorward of the boundary; this is an artifact of the reconstruction process. The arc

boundary, as observed by the in situ electron precipitation measurements, spans less than 0.06° (3–4 pixels in the model space). The arc length is wider than the model space (128 pixels, 6° longitude). The aspect ratio here is more than 30; neither the smoothing done in the constrained vector fit, nor the long narrow basis functions of the arc-aligned scalar fit reconstructions, are able to capture the sharp boundary.

3. Campaign Overview and Model Input Data

The Isinglass campaign provided high-resolution in situ measurements of plasma flow in the context of ground based cameras and radar observations. The example shown in Figure 1 is one timestep from case c5 of the four event studies, listed in Table 1, which we examine with the GEMINI model. Under the assumptions (Section 1) of slowly time-varying arcs and along-arc invariance over the model grid space, we create four separate case studies with time-dependent electric field data and precipitation data maps to be used as drivers for the GEMINI model. As in Clayton et al. (2019), we apply the replication and reconstruction process to PFISR-based vector flow measurements, and to in situ DC electric field measurements, for two separate events on the night of March 02, 2017. The earlier event, 0704 UT (data set c1), has only PFISR radar data available, but presents a straightforward case study of the behavior of quiet stable arcs. The second event, 0753 UT (data sets c3, c5, and c6), was just after the launch of the second of the Isinglass rockets, 36.304, and allows another case of a stable arc, formed shortly after a substorm. For the second event, we have both in situ measurements of the flows around the arc structure, and PFISR radar observations of the same. The four flow-field and precipitation-inversion data set we will be using to drive the model are (c1) a PFISR-based map of the 0704 event, (c3) a PFISR-based map of the 0753 event, and (c5 and c6) two versions of in situ based datamaps of the 0753 event. The two in situ datamaps are a result of different methods for the reconstruction processes of the in situ electric field data, which yield similar but slightly different results.

The PFISR data used for c1 and c3, and the in situ data used for c5, are reconstructed with the constrained vector fit process described above. Here, the input field data are densely replicated at many places along the arc, allowing the divergence-minimization constraint to find a suitable solution. Note that for c5, there is only one “set” of originating data, along the trajectory of the rocket flight. Thus only one full reconstruction is done, combining the full trajectory of data with the arc boundary at T+075240, nearest the time when the rocket crosses into the arc. For other time frames of case c5, GEMINI is run with a version of that flow field which translates across the model space based on the latitudinal motion of the center of the arc boundary. For c6, the c5 reconstruction is taken as an input, and then the arc-aligned scalar fit process is applied to that for reconstruction. In this c6 case, the arc boundary used at each time step follows the imagery data for each time step. Future uses of the arc-aligned scalar fit process will (a) correct small errors in the calculation, (b) will work directly with the original vector data (rather than with the c5 flow field as is done here), and (c) will optimize the combination of basis functions and parameter searches.

The PFISR data used come from the “VVELS” (reconstructed vector velocity) database (Heinselman & Nicolls, 2008); the PFISR radar was run in a dedicated 15-beam mode during this campaign, as detailed in (Fraunberger et al., 2020). In situ flow data use an absolute reference frame despin of the COWBOYS (Cornell Wire Boom Yo-Yo) electric field measurements (Klatt et al., 2005) using the lower cadence (≈ 1 Hz) thermal ion flux PIP (Petite Ion Probe) data for directional information (Fraunberger et al., 2020). All of these model runs are also driven by camera-based inversions from filtered cameras based at Venetie for the particle information (Grubbs, Michell, Samara, Hampton, & Jahn, 2018), as detailed in (Clayton et al., 2019). The onboard in situ fluxgate magnetometer for Isinglass was as described in Lynch et al. (2015) for the MICA (Magnetosphere-Ionosphere Coupling in the Alfvén resonator) rocket.

Figure 5 shows a sample of the model-driving data sets of the electric field (shown as flow components) and particle drivers, together with the associated arc boundaries used for replication of the field data. One time step is shown, for the c1 and c5 time sequences. (The same flow data are also shown in Figure 3 in an HSV representation.) The arc of interest is visible for each event, just poleward of the marked auroral boundary line, as a rotation in the fields/flows (as expected from Equation 1), and an intensification in the particle measurements (entry into the precipitation region). For c5 (and thus c6), the rolloff of the field variation near the arc boundary is apparent; compare to the original data shown in Figure 4. The c1 data set has a 2 s

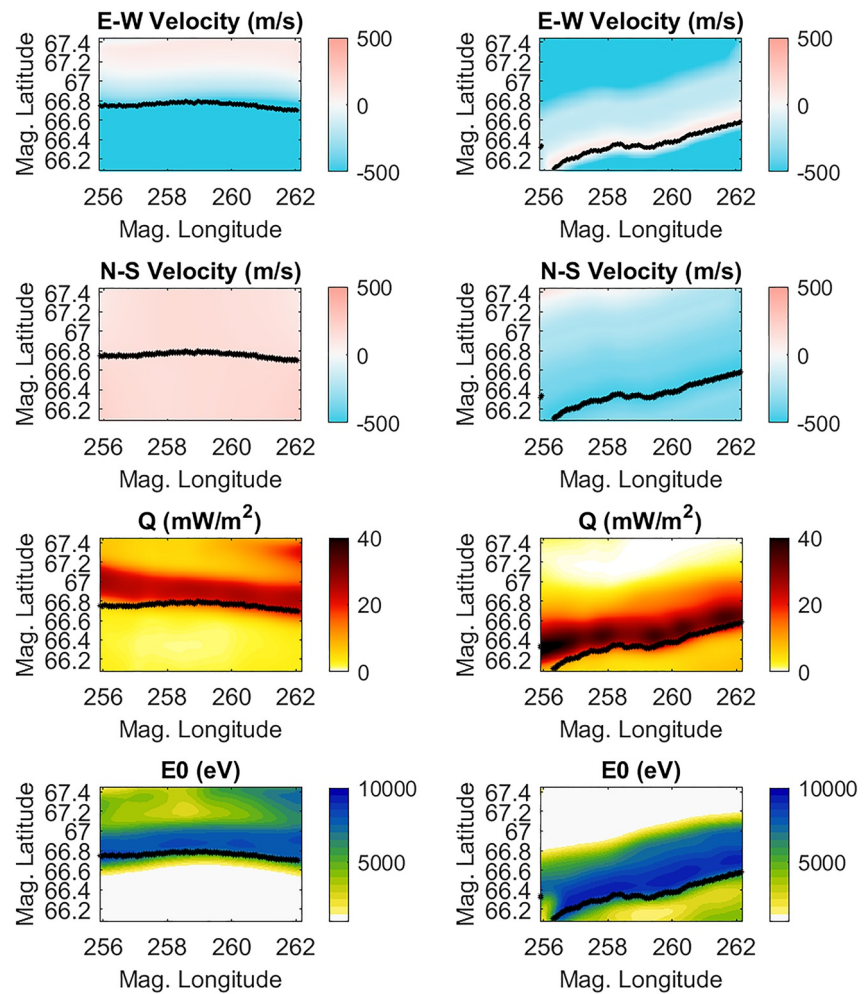


Figure 5. 2D model inputs for Geospace Environment Model of Ion-Neutral Interactions, cases c1 and c5 example timeframes (0704 UT and 075245 UT). The upper panels show the east-west and north-south components of the flow field in geomagnetic coordinates; the arc boundary is overlaid in black. The lower panels show the energy flux (Q) and average energy (E_0) from camera inversions.

cadence, and the c3/c5/c6 data sets have a 5 s cadence. Time sequences of these input drivers can be found in the Supporting Information S1 for each of the four model runs.

4. Model Outputs

Driving the GEMINI model with the inputs exemplified in Figures 3 and 5 yields four output volumetric data sets of the 3D structure around an arc, including currents, conductivities, and density structures as a function of time. Example timeframes from the four model run outputs are summarized as matching sets of panels in Figures 6 and 7-c1, -c3, -c5, and -c6. The Supporting Information S1 includes all of the timeframes. Visualizing the volumetric output with 2D slices through the 3D model volume can help us understand the differences between each run. These visualizations provide worthwhile insight into the process of ionospheric current closure. Keep in mind though that they are simply 2D slices through 3D (and time-dependent) volumes of each parameter; Figure 1 illustrates another, 3D, visualization of one time step of the currents for run c5.

The large center panel of each case of Figures 6 and 7 is a slice through the model volume in the magnetic latitude/longitude plane, at 100 km altitude, of the electron density. The panels to either side are slices in the altitude/magnetic latitude direction, along the red dotted line in the center panel. The left panels show

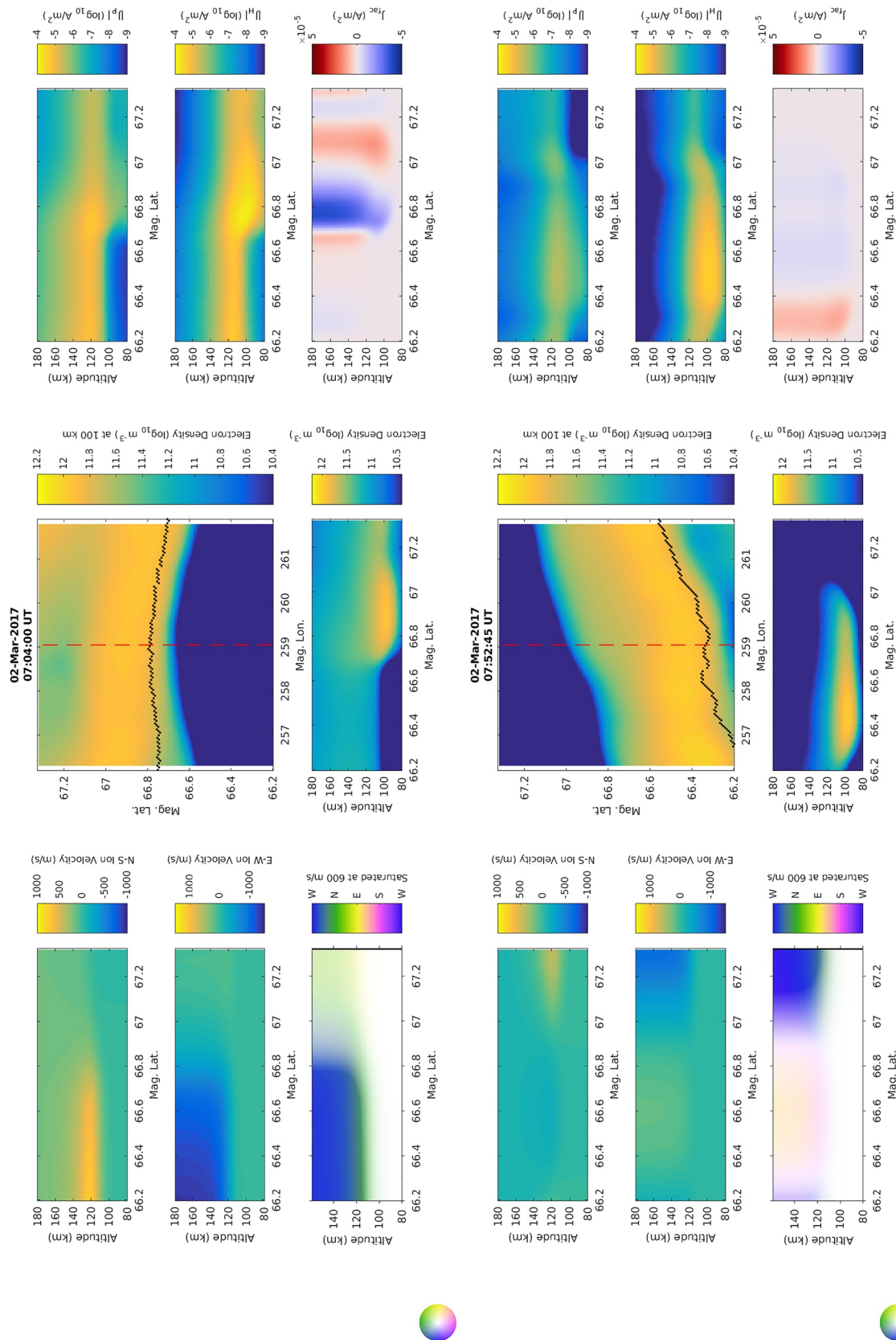


Figure 6. Geospace Environment Model of Ion-Neutral Interactions (GEMINI) calculated model outputs for the four GEMINI runs, see text for details. Panel sets c1, c3, c5, and c6 show parallel composite plots at nominal timeframes for each of the four GEMINI model run outputs, summarizing density, velocity, and currents in various slices of the modeled volume. Precipitating-electron current (negative) is shown in blue; return current is in red.

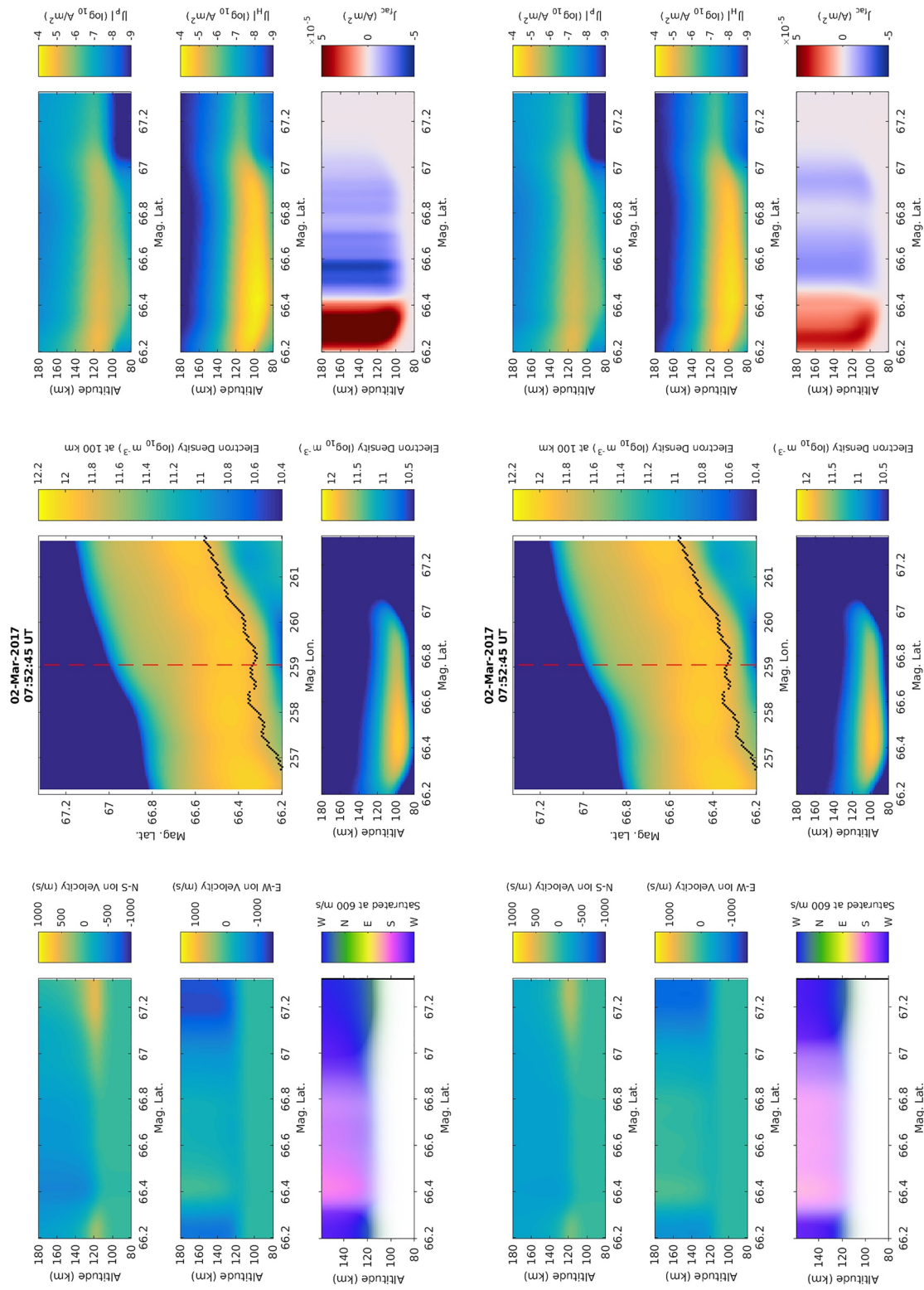


Figure 7. Continuation of Figure 6.

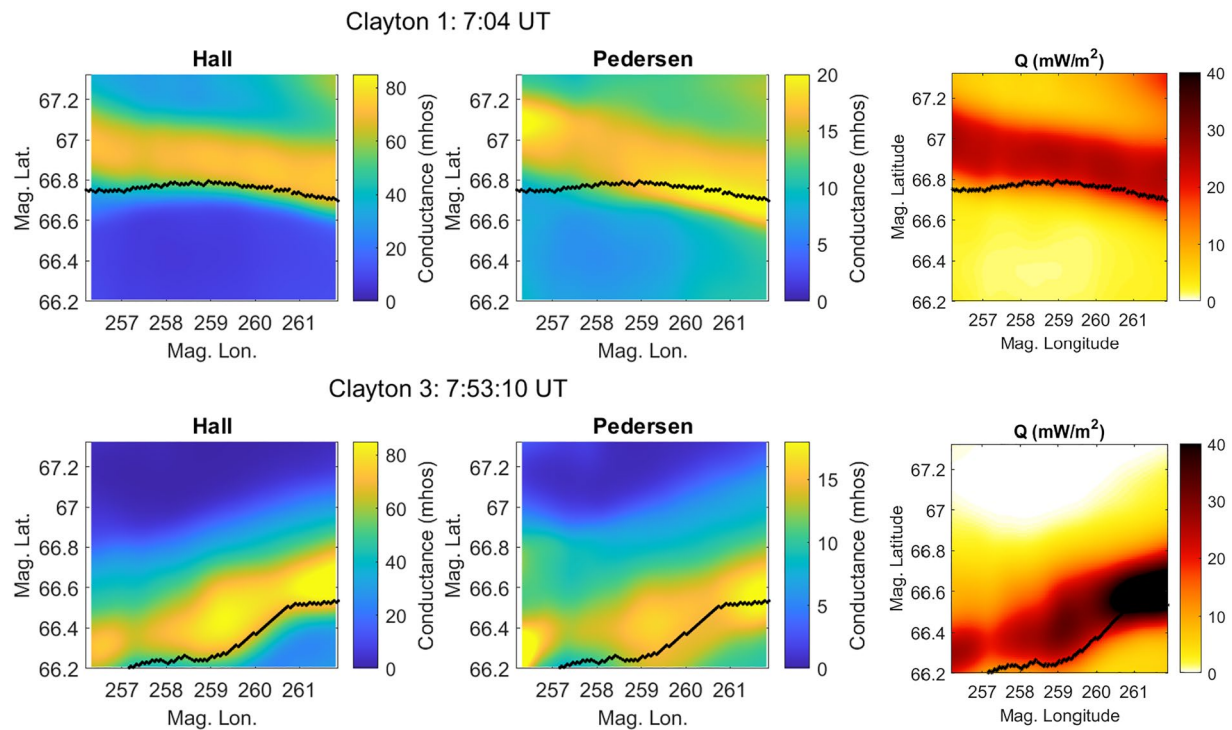


Figure 8. Height-integrated conductances for comparison to Q from inverted imagery, indicating Pedersen transport. Note that c3 timeframe shown here is 075310, later than the nominal example timeframe to allow the transport time to develop in the model.

the components of perpendicular ion flow, with the E/W and N/S components visualized first separately, and then together as an HSV representation similar to that of Figure 3 (although here, in the altitude/latitude plane rather than in the horizontal plane). The right panels show the currents for this time step, as a function of altitude and magnetic latitude, in the Pedersen, Hall, and field aligned directions. We remind the reader that negative (blue) field-aligned currents indicated currents from precipitating auroral electrons; return currents (positive) are shown in red. The lower center panel shows an altitude/latitude cut of plasma density.

Comparing the density and flow outputs here, and the inputs and arc boundaries in Figure 5, we can see clear changes/rotations in the flow and increases in the density at the location of the arc boundary. On the right panels of Figures 6 and 7, note the altitude difference between the Hall and Pedersen current peaks, ~ 100 and 120 km altitude, respectively. Field aligned currents extend down to 100 km altitude indicating that they are at least partly sourced from the Hall currents.

Often the field-aligned current signatures show a narrow channel of downward current that changes into upward current below 120 km. For example in Figure 6-c1, at $07:04$ UT and 66.67 MLAT, we see a significant Hall current variation, and the upward and downward field aligned currents show a vortical structure in the vertical and cross-arc direction. This is an indication of a vortical current structure. The strong Hall currents in the E-region are consistent with previous modeling investigations by Mallinckrodt (1985); similar signatures are noted by Fujii et al. (2011). The vortical current structures modeled by Mallinckrodt (1985) were the result of polarization electric fields that develop within an auroral arc to maintain current continuity (e.g., G. Marklund, 1984; Paschmann et al., 2003); these polarization electric fields can also connect to field aligned currents (Mallinckrodt, 1985). On the left panels, it is interesting to note the altitudinal dependence of the flow vector directions; flow at the top of the model space is imposed by the electric field map driver (equipotentials along field lines throughout the model space), but in the lower altitude ionosphere, the flow rotates sharply below 120 km altitude from collisional effects. This is most apparent in the southern half of the c1 event, between 110 and 120 km.

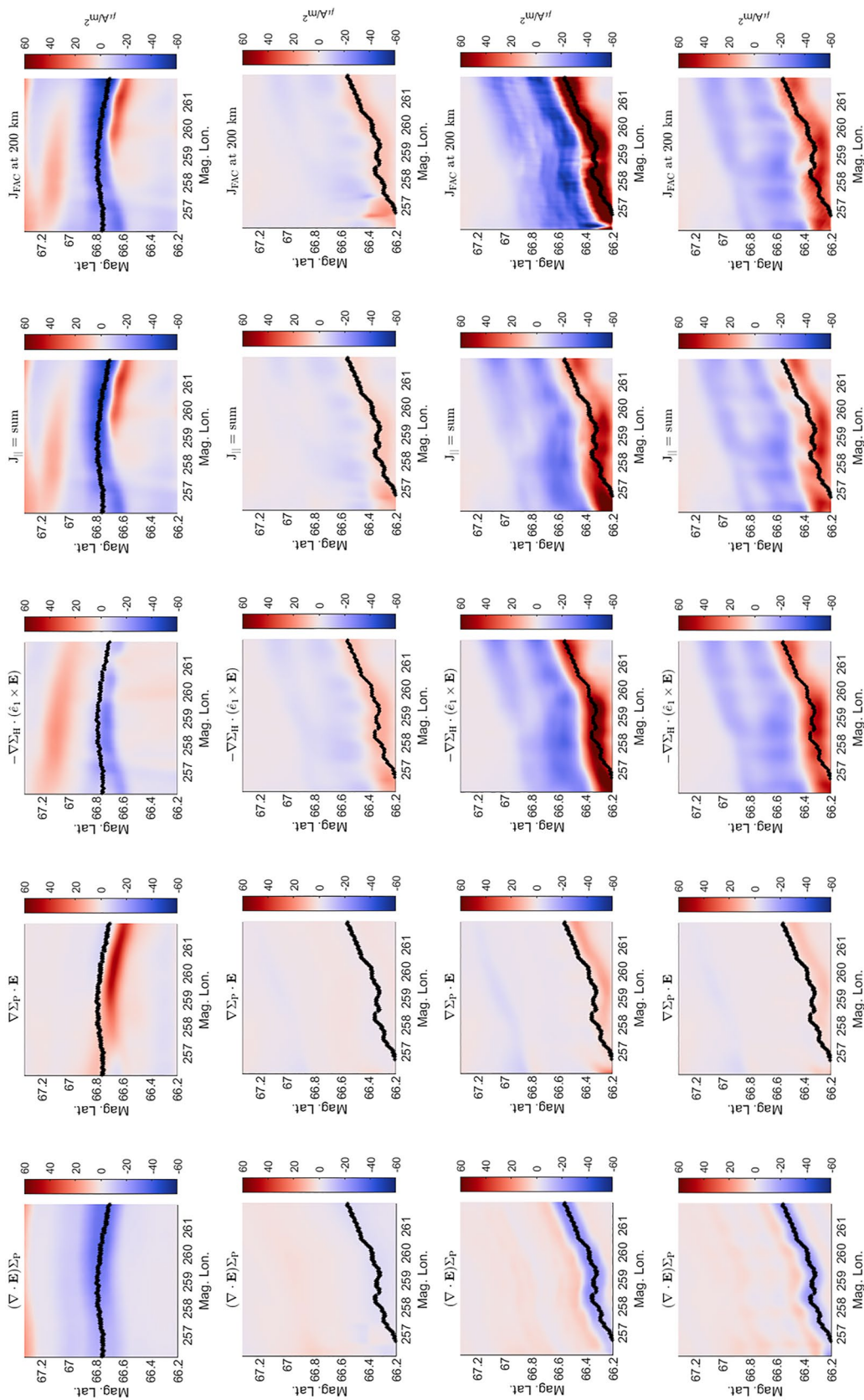


Figure 9. Comparisons of field aligned current contributors from c1, c3, c5, and c6 outputs. Terms of Equation 1 are calculated from the model output and overlaid with arc boundary marker in black. Right columns show sum of height-integrated contributors (“sum”) and (far right) volumetrically calculated J_{FAC} at 200 km altitude. Axes are magnetic longitude (λ) and latitude (ψ).

The relative locations of density, current, and flow structures are the result of the full transport calculations by GEMINI. While Equation 1 provides expectations for overall height-integrated effects (i.e., conductances), GEMINI calculates behavior (i.e., conductivities) at each point in the 3D volume. Our simulations show evidence that transport is playing some role in redistributing plasma in the E-region. Pedersen drifts (which can be compressible) can result in production of density cavities and regions of enhancement on top of what is provided by impact ionization (Doe et al., 1995; M. Zettergren & Semeter, 2012). Transport effects evaluated through the divergence of the ion flux (not shown) confirm that this process plays some role in the events we model. It acts to move plasma in the direction of the electric field such that the peak Pedersen conductance is displaced somewhat from the region of maximum precipitating energy flux, as is shown in Figure 8; at the right hand edge of each example, the Pedersen conductance can be seen to peak roughly 0.1° equatorward of the energy flux.

While GEMINI provides new insight into volumetric processes, it is an additional validation to height-integrate its volumetric output and compare it to expectations for the height-integrated Equation 1. The terms in the height integrated current continuity equation detailed in Equation 1 can be calculated from the model output, and are represented in Figure 9 for the four example cases, and compared to GEMINI calculations of the field-aligned current (see the second paragraph of Section 2) sliced at 200 km altitude. Calculating j_z from summing the values of the terms in this height-integrated equation should reproduce the current calculated by the model under the assumption that the input electric field is truly curl free (since Equation 1 ignores the $\nabla \times \mathbf{E}$ term). The degree to which this summation does not match the model-generated field-aligned current is a metric to show errors resulting from processing data into model inputs, and in particular, how residual curl in the driving electric field data sets for c1, c3, and c5 affects the output. We can see that the general shapes and magnitudes of the parallel current are reproduced by the summation of the height-integrated current continuity terms, but some of the striations in the model output are not present in the calculations based on Equation 1. This issue is most apparent in the c5 simulation case where a quick glance at the two rightmost panels of the third row of plots reveals significant differences. This could imply that some non-idealized non-curl-free measurements in the arc (e.g., from Alfvénic fluctuations) are being replicated, but shows that any residual effects from their presence are relatively modest compared to the larger scale DC features in the parallel current.

Separately, we have also run c5 and c6 simulations again but with all curl explicitly removed from the GEMINI input data. This is accomplished by performing line integrations of the field and then numerically taking the gradient of that potential to approximate a curl-free field. This exercise allows us to assess the possible impacts of residual curl and restrict our attention to features that are not an artifact of this curl. Fully curl-free simulations (included in the Supporting Information S1) are, of course, somewhat different from those presented here; nevertheless the major features of the currents systems remain similar to what is seen in version of c5 and c6 included in this paper so we do not discuss these further.

For each of the data sets in Figure 9, notice the locations of the positive and negative field aligned current (right columns) with respect to the location of the equatorward arc boundary, where here again negative J_{fac} (field aligned current, the j_z of Equation 1) is precipitating-electron current, and positive is return current. We see that for each event depicted, the precipitating-electron current region lies poleward of the equatorward arc boundary. The return current region can lie either equatorward or poleward of the precipitation region. Note the relationship of the $\nabla \Sigma_H$ and $\nabla \Sigma_P$ terms of the continuity equation in the second and third columns of Figure 9, to the arc boundary location.

Particularly here, we note the artifact of the flow field processing mentioned before in the discussion of Figure 4, whereby the flow field appears to vary equatorward of the arc, contrary to the originating in situ data. In the c5 and c6 cases, the divE contributor term appears to show a negative FAC contribution equatorward of the arc boundary. This is an artifact of smoothing of the flow field, causing variations of the flow on both sides of the arc boundary. The sharp blue signature is actually a contribution that exists poleward of the arc boundary.

For these events, the return current is dominantly sourced by conductance gradients, including that of the Hall conductance. In a previous study (Lynch et al., 2015; M. Zettergren et al., 2014), the divergence of \mathbf{E} term accounted for both the precipitating-electron and return current regions for a rapidly varying surge

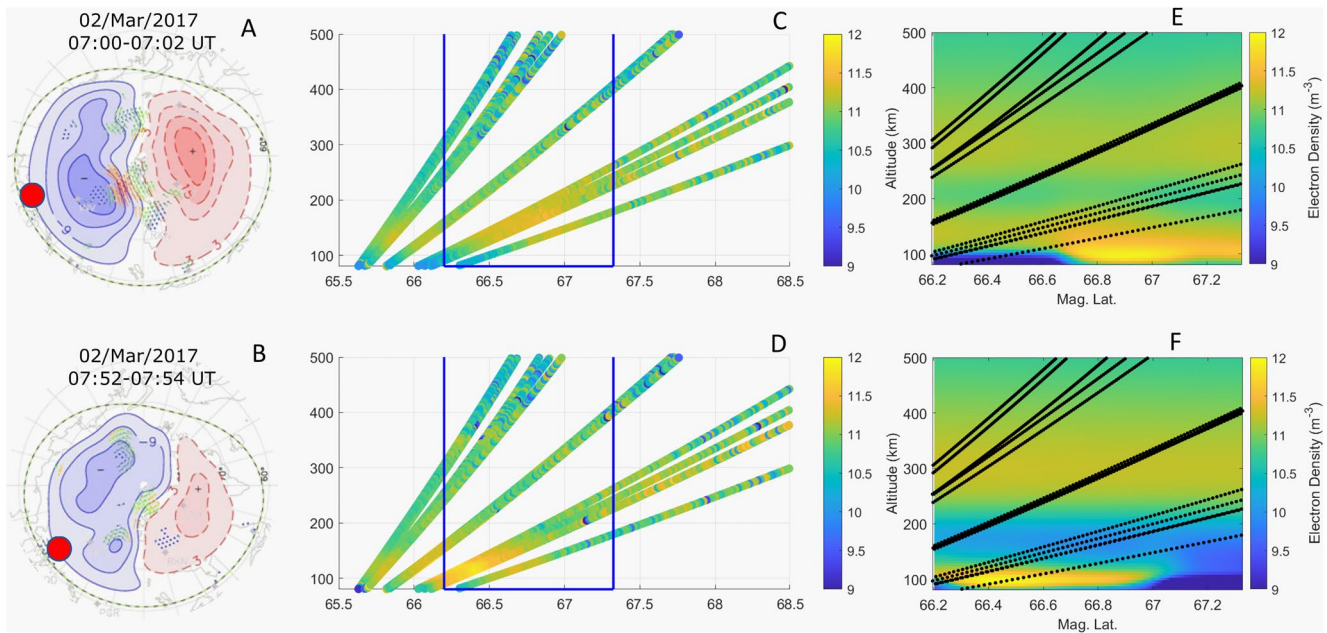


Figure 10. (a, b) SuperDARN convection cell maps for events c1 and c3/c5/c6. (c, d) Poker Flat Incoherent Scatter Radar density as a function of latitude/altitude. (e, f) Geospace Environment Model of Ion-Neutral Interactions density through F-region for c1 and c3.

event, indicative of a smooth conductance with minimal localized gradients. For this present study, conductance gradients appear to play a stronger role.

The first two model runs (c1 and c3) are driven with PFISR-based flow data, and exhibit larger feature sizes and overall lower current values than the in situ field-driven counterparts (c5 and c6). In addition to the differences in scale, the PFISR-based data have a temporal ambiguity (66 s cadence) which, for these moving arcs, leads to a location ambiguity of the driving data on the order of the size of the PFISR pixels (roughly a quarter of a degree in latitude, large compared to the definition of the auroral boundary). In the next section, we compare and contrast details of current features and decomposition into current continuity equation components, as well as differences in the values and scale sizes of the PFISR-based and in situ-based model run output parameters.

5. Discussion

We begin with an overview comparison (review the rightmost column of Figure 9) of the model-generated field aligned current structure for each model run. In the text below we will work through two comparisons between the model outputs shown in Figures 6, 7, and 9. Revisiting the top two rows of Figure 9, Comparison One is between the PFISR-driven runs during the 0704 event (data set c1) versus the 0753 event (data set c3), highlighting the differences between two different auroral events as illustrated in the model output. In particular, we see how variations in the arc structure cause differences in the importance and location of the Hall and Pedersen conductance gradient terms of Equation 1. Comparison Two (the bottom three rows of Figure 9), between the three model runs of the same event (0753, data sets c3, c5, and c6), explores the effects of different field driver resolutions and processing for the same event. Comparison Two illustrates the strong dependence of the output current strengths, on the resolution of the input field drivers. Compare the rightmost column of Figure 9 to the inputs in Figure 3. Note that sharp features in the input flow fields correspond to strong features in the modeled output current, as might be expected.

5.1. Comparison One: 0704 Versus 0753 UT, Run With PFISR Flow-Field Data Input

Comparing the events at 0704 UT and 0753 UT (Figure 6 c1 and c3 and Figure 9 c1 and c3), both using input flow field data from PFISR together with inverted imagery, provides a comparison of two separate events

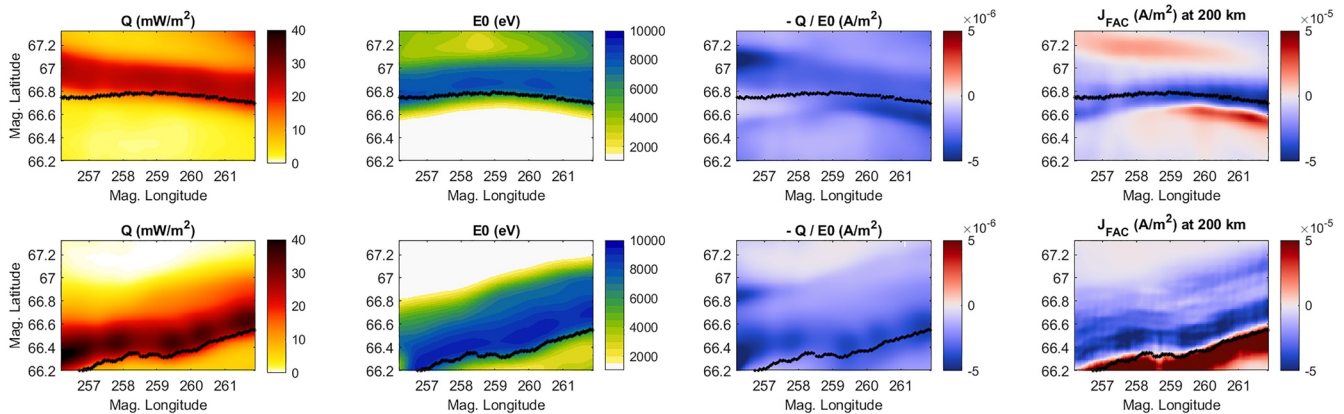


Figure 11. Negative j_z (precipitating electrons) represented from camera inversions as $-Q/E0$ for the 0704 UT (c1) and 075245 UT (c3, c5, and c6) in situ events; compared to Geospace Environment Model of Ion-Neutral Interactions generated current profiles for c1 and c5. Note the different color bar limits in the third versus fourth columns.

with equivalent-resolution data drivers. The 0704 event occurs after a long period of relative stability of quiet early evening auroral arcs, whereas the 0753 UT event occurs immediately after a substorm has moved through the area, and a stable arc re-organizes over the field of view. We can see strong effects from the conductance gradients in both events, a feature of these arcs that was not evident in the Lynch et al. (2015) study. We see in both cases here that the precipitation region of the arc is related to the divergence of the electric field, and that both the precipitation and return current regions are linked to the conductance gradient terms. For the 0704 event, the Pedersen gradient dominates the return current, whereas for the 0753 event the Hall gradient is dominant. For both events, conductance gradients feed the return current.

The importance of the conductance gradient terms is of interest, particularly in contrast to previous events (Lynch et al., 2015) where the divergence of the electric field term was seen to be of primary importance; both of the events in Comparison One have the return current region highly dependent on the conductance gradient terms of the current continuity equation. In the Lynch et al. (2015) event, the arc was moving southward at 22.5°/hr (0.7 km/s); for the 0704 event here, the southward motion was 3.5°/hr (0.11 km/s), and for the 0753 event, it was 4.5°/hr (0.14 km/s). These slower Isinglass event velocities are in the reported range of equatorward drift velocities of growth phase arcs (Karlsson et al., 2020). The rapid motion of the Lynch et al. (2015) event makes it plausible that a uniform-conductance ionosphere is less affected by the precipitation, while in the c1 and c3 events here, with their more slowly propagating precipitation structures, the ionospheric density (and conductivity) profile is more affected by the presence of the arc. With regard to the various stages of aurora defined in Marghitu (2012), neither the MICA nor ISINGLASS events can be suitably classified as quiet since both occurred in an expansion phase; these may correspond to the transient stages 2 and 3 of Marghitu (2012). Our analysis certainly suggests that the Hall current plays a substantial role in the conditions we observe.

We consider the differences and similarities between the c1 versus the c3 events to understand the importance of the Hall versus the Pedersen conductance gradient term. Some external diagnostics available include SuperDarn convection patterns and PFISR density profiles, shown in Figure 10. The SuperDarn convection context can provide a large-scale view of the environment of each event, and the PFISR-based density measurements of the region around the arc can be compared to GEMINI-generated density volumes.

In the left panels of Figure 10, we note differences in the large scale convection patterns over the regions seen/modeled by SuperDARN especially in the region near Poker Flat AK. In our local data sets (Figures 2 and 3), the c1 event is a much more sheet-like arc with a shear flow pattern, whereas the c3 event has some along-arc variation and across-arc flow components. The c1 event arc is more parallel to its adjacent flows, and is magnetic-latitude aligned. The c3 event is not magnetic-latitude aligned, has along-arc variation, is located in a distorted convection cell potential visible from SuperDARN, and has an increased importance of the Hall term equatorward of the arc. Additional cross-arc flow in event c3 has increased the importance

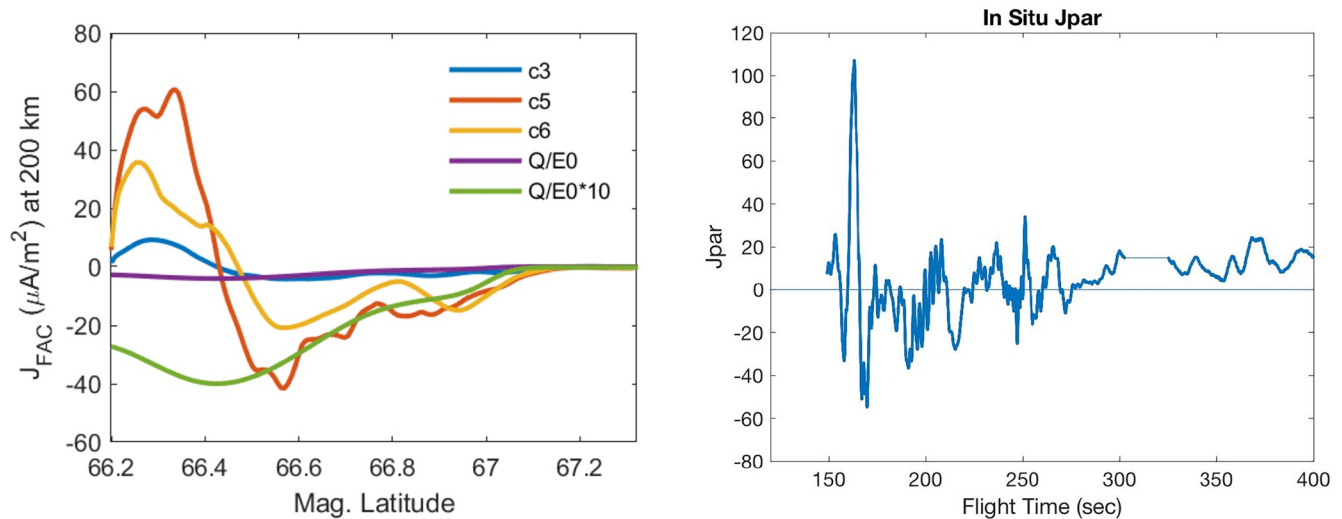


Figure 12. (Left) Cuts through the model domain, for runs c3, c5, and c6, along the central magnetic longitude for parallel current, overlaid with imagery inversion cuts ($\times 10$); compared to (right) in situ measurements (in $\mu A/m^2$). Flight time of 150 s corresponds roughly to magnetic latitude of 65.98° ; 250 s, to 66.41° ; and 350 s, to 66.85° .

of the Hall gradient term in the current continuity equation relative to the Pedersen term. Quiet arc structures are generally quite well aligned to local convection patterns (Gillies et al., 2014), and it is worthwhile to note here the combination of the deviation from an idealized system, with the increased importance of the Hall conductance gradient term.

One of the important consequences of current closure through the Pedersen current is the dissipation of energy through Joule heating. Pedersen current closure associated with auroral arcs has been investigated observationally (e.g., Dahlgren et al., 2014; de la Beaujardiere et al., 1977; G. Marklund, 1984; G. Marklund et al., 1982; G. T. Marklund et al., 2001) and through modeling investigations (e.g., Doe et al., 1995; Karlsson & Marklund, 1998; Mallinckrodt, 1985). However, as shown in Equation 1, the closure of field aligned current through gradients in the Hall conductivities is an alternate pathway. Closure of currents through the Hall conductivities has been sparsely studied (e.g., Sugino et al., 2002). As pointed out by Amm et al. (2008), the details of current closure have important implications for energy deposition because Hall currents do not dissipate energy. For the 0753 cases (c3, c5, and c6) of our investigation, we find that closure of field aligned currents associated with Hall conductivities occurs where the aurora is less sheet-like, as compared to the 0704 case (c1) where the aurora was relatively east-west convection-field aligned, sheet-like, and dominantly described by Pedersen closure.

This modeling suggests that the spatial structure of slowly moving aurora has an important impact on the closure of field-aligned currents, through either Pedersen currents during less structured aurora or Hall currents during more structured aurora. Current continuity maintenance during more structured auroral configurations here requires dissipationless Hall currents. One possible scenario is that the energy dissipation provided through the Pedersen current and Joule heating may reach maximum magnitude and thus the Hall current is also needed to maintain current continuity. This perspective is also supported by the fact that the Pedersen conductance can effectively plateau in magnitude, that is $\Sigma_p \propto \sqrt{Q}$, where Q is the energy flux of the auroral precipitation (Kaepler et al., 2015; Robinson et al., 1987); this effect depends on the average energy, as shown in Marghitu et al. (2009).

Separately, we consider the electron density profiles observed with PFISR relative to the electron density produced by the GEMINI model for case c1 versus c3, as shown in the middle and right columns of Figure 10, respectively. The GEMINI-calculated electron density enhancement associated with the auroral arc is consistent with the PFISR observations, which show an ionization enhancement at low altitudes when the enhancement is within the beams' field of view. Both events show some evidence of Pedersen transport in their GEMINI calculations, as discussed above concerning Figure 8.

5.2. Comparison Two: Different Scale Flow-Field Drivers at 0753 UT

Next, we more thoroughly analyze the 0753 UT event traversed by the Isinglass rocket, using different flow-field drivers to see how the resolution of the data-driving model inputs affects the 3D model GEMINI output. We can compare the GEMINI calculated field aligned currents in the three 0753 cases (c3, c5, and c6), to available independent metrics: inversion of the filtered imagery, and deconvolution of the onboard magnetometer. The particle drivers for these three model runs are all the same, sourced from the average energy and energy flux data inversion maps from the filtered cameras. The flow field drivers, however, come from different sources, and processing, of ionospheric flow data available for the 0753 UT event. Compare the last three sets of plots in Figures 6, 7, and 9 to see the PFISR-radar-driven (c3), in situ-driven with divergence-constrained vector flow fit (c5), and in situ-driven with arc-aligned scalar flow fit (c6) model results. The three different cases show similar electron density model outputs, which is to be expected as that calculation is driven primarily by the camera inversions (the same for these three simulations.) However, the three model runs calculate strongly different current density outputs; in particular, the current density magnitudes between the PFISR-driven and in situ-driven simulations. To assess the varying calculated currents from these three different model runs, we can compare to camera inversions, and to in situ magnetometry.

Using the camera inversions to calculate j_z can give us a comparison metric for the GEMINI-calculated precipitating-electron j_z in the arc, but will only include particles that result in distinct optical signatures, not thermal or near-thermal electrons which are subvisual current carriers. Figure 11 shows this for the 0704 and 0753 cases. Here, the positive values associated with the GEMINI return current system should be ignored in the comparison, as they will not be represented by the camera inversions which only capture light from the precipitating electrons. These panels show a severe underestimate (note carefully the color bars of the rightmost two columns) by the camera inversions of the magnitudes of the parallel current in both events; while the c3 calculations (shown in Figure 9) are lower than these c5 calculations, even they, like c1 here, far outpace the camera inversion value.

In order to quantify the comparisons between each case, we can take cuts through the model domain for each simulation and overlay them. Figure 12 shows the j_z from the PFISR-driven (c3), in situ-driven (c5), and arc-aligned scalar fit (c6) runs cut along the central longitude, together with a matching cut from the optical inversion (multiplied by 10). Note that the optical inversion used here (Grubbs, Michell, Samara, Hampton, & Jahn, 2018), while making some corrections for a low-energy tail, provides a value for Q which is dominated by a single Maxwellian particle distribution. A previous multi-rocket auroral study (Arnoldy, 1977) indicated that much of the field-aligned current from auroral precipitation is carried by electrons below a keV near the edge of the visible arc. Figures 4 and 12 here seem consistent with this conclusion; thus the dominant current carriers are excluded from this optical inversion through the 1 keV floor of this optical inversion calculation. It remains intriguing that despite the shift in magnitude, the camera inversions for these cases match the spatial profiles of the GEMINI calculations quite well in both cases. There is no reason to expect that the distribution of precipitating-electron current carried by subvisual electrons should be proportional to that of the visible carriers.

Next, we can compare the GEMINI currents to deconvolutions of the onboard magnetometer. Figure 12(right) shows the j_z inferred from the in situ magnetic field measurement $\nabla \times \mathbf{B}$ along the rocket trajectory assuming a stationary sheet-like arc.

For the in situ driven cases c5 and c6, there is agreement between the location and values of the model output current and the in situ magnetometry measurements, though the model output does not capture the sharpness of the in situ signatures. The PFISR-based run (c3) shows similar overall features to the in situ runs, such as the presence of the arc, but shows even more smoothing over the fine scale features through the arc, and thus has damped magnitudes of the model outputs at all latitudes. The large averaging in space and time for the PFISR electric field data is not able to reproduce the peak magnitudes of the electric field drivers from the in situ measurements, thus providing an underestimate of the peak driving fields, and resultant currents, for the GEMINI model.

Even with an underestimate of the field magnitudes, the PFISR-driven data are still able to reproduce both the same large scale features present equatorward and poleward of the arc boundary, as well as the same relative importance of the terms in the current continuity equation for sourcing the precipitating-electron

and return current regions, as do the in situ data-driven runs. This consistency is interesting and important, showing that even if the model is driven by different sources of field data (that may not even agree in relative magnitude) it can reproduce the same relative importance of each aspect of the current closure system.

6. Conclusions

Modeling the 3D environment near an arc structure can account for the 3D dependent terms of the continuity equation which controls the ionospheric current closure system. This 3D volumetric calculation adds along-arc, non-sheetlike, not-height-integrated physics to the interpretation of auroral systems. The differences between the slow time varying Isinglass campaign events to the rapidly moving MICA event (Lynch et al., 2015; M. Zettergren et al., 2014) illustrate when there is need to consider the gradient of the conductance terms for current continuity. For growth phase arcs moving at 100 m/s equatorward drift velocities, the conductance gradient terms of Equation 1 can be dominant. For both sheet-like and slightly non-sheetlike arcs, the conductance gradient terms can play an important role in the determination of the return current region. Additionally and importantly, we see that consideration of Hall conductivity gradients can be necessary for even limited excursions from sheet-like magnetic-latitude-aligned arc structures. These modeling results show that the Hall currents during structured auroral events can become a significant pathway for current closure, independent of energy dissipation requirements into the ionosphere-thermosphere system.

In this Isinglass-GEMINI study, we have created localized flow maps over a region near an arc, and converted these maps into detailed descriptions of auroral currents yielding a comprehensive view of ionospheric signatures of auroral system current closure. We showed that radar-driven model runs produce quantitatively smoothed, but qualitatively similar, current maps. The radar-driven runs show the same relative importances of the various current continuity terms as do the in situ-driven runs, but severely underestimate the current densities because of large beam spacing leading to unresolved gradients. Data-driven modeling results also indicate that Pedersen transport significantly affects the distribution of plasma density in the E-region in and around the auroral arc; this process manifests as a displacement of the density peak, around 120 km altitude, in the direction of the electric field, away from the region where the total energy flux maximizes.

We compared various aspects of the GEMINI calculations to independent measurements. While parameters with short-lived “time constants” like current density and E-region ionization are well-captured in our simulations, longer lived features like F-region density structures cannot be captured well as these partly result from transport of plasma from outside the modeled region. Such F-region transport does not affect electro-dynamics overmuch but is interesting in its own right. Addressing F-region structures from a local-scale modeling point of view is challenging and requires actively setting inflow boundaries using perhaps data from PFISR or a global-scale model—clearly a substantial and useful task that may prove fruitful for future studies.

Future applications seeking to improve and expand the driving inputs to the 3D GEMINI model beyond these longitudinally constrained examples will leverage better capabilities for flow-field imaging, either via new radar systems (EISCAT3D) or swarms of satellites. That is, we can use similar techniques with multi-satellite passes (or EISCAT3D) over comparable ground instrumentation, such as with the proposed ARCS ionospheric swarm of CubeSats over an array of filtered ground based imagers. Using multipoint satellite passes (or EISCAT3D) over the same region, rather than by replicating single cuts as is done here, can replace the reconstructed replicated-data maps with reconstructions from truly distributed observations.

Appendix A.: Arc-Aligned Scalar Fit Reconstruction Method

For these reconstructions, a scalar basis function representation for the electrostatic potential field is found which gives a flow field consistent with the auroral boundary, and with the available data. The component of the flow along the magnetic field is assumed to be zero, allowing the flow to be understood as a two-dimensional vector field; here we are discussing the F-region top-boundary model driver. Two-dimensional, divergence-free vector fields can be represented as the rotated gradient of a scalar field (the cross product of the gradient vector with a unit vector parallel to the magnetic field). Using this representation, a scalar func-

tion is fit to the flow information. Basis functions for the scalar were designed to enforce minimal variation along the direction of the arc boundary. The final set chosen were “sloped ridges” running parallel to the arc boundary from one side of the area of interest to the other, with Gaussian profiles perpendicular to the arc and linear profiles parallel to the arc. The width of the Gaussians is specified for each run depending on the level of granularity desired in the fitting. Sharper ridges allow more detailed reconstructions. The spacing of the ridges perpendicular to the arc is optimized to be just close enough together that a flat area can be constructed by two adjacent peaks set with equal weights. “Parallel to the arc” is defined to be the direction along lines of equal distance from the arc boundary, while “perpendicular” is correspondingly taken to be the direction of maximum increase in distance from the arc boundary. The rotated gradient fields of the scalar potential are minimized to the flow data, yielding separate coefficients for each ridge function. Because the arc boundary information is incorporated into the fit, flow information can be reconstructed across large gaps in the data without risk of artificial loops or eddy structures forming in the gaps between data points as a result of insufficient constraints on the fitting. The result is a smooth analytical flow function in two-dimensions that can be sampled at any desired point. In the examples included here, eight ridges were included per degree of magnetic latitude, for 13 ridges in total. The shape term was fixed such that for evenly spaced ridges, the scalar function would be flat across the area of interest if all of the ridges had the same weighting. The position of the ridge was taken as one of three parameters for the fitting, along with maximum value of the ridge and its slope parallel to the arc. This allows the ridges to bunch around areas of sharper change.

Acknowledgments

Isinglass analysis work at the Dartmouth College was funded by UNH/NASA ESPCoR NNX15AK51A, Space Grant NNX15AH79H, and LCAS Isinglass NNX14AH07G. The Isinglass team thanks the engineering groups at the NSROC, the NASA Wallops, and the PFRR, for their hard work and dedication to sounding rocket missions. This project was aided by the SRI/PFISR and the UAF/GI staff at Poker Flat Research Range, as well as Dr. Mark Conde’s (UAF/GI) Scanning Doppler Imager (SDI) facility. PFISR operations are supported by the NSF cooperative agreement AGS-1133009 to the SRI International, and all PFISR data are available through the Madrigal database (isr.sri.com/madrigal). The authors acknowledge the use of SuperDARN data (vt.superdarn.org). SuperDARN is a collection of radars funded by national scientific funding agencies of Australia, Canada, China, France, Italy, Japan, Norway, South Africa, United Kingdom and the United States of America. The authors acknowledge the use of the convection mapping tool hosted by the Virginia Tech SuperDARN group at their website (<http://vt.superdarn.org/tiki-index.php?page=Conv+map+overview>). R. Clayton and K. A. Lynch would like to thank Laura Petto and Prof. Anne Gelb of Dartmouth Math department for guidance on CVX optimization. The authors also thank Mike Fraunberger for his work on the Isinglass in situ measurement data. M. Zettergren acknowledges the support of the NASA grant NNX14AH07G and use of the ERAU Vega High-Performance Computing Cluster for running simulations presented in this paper. M. Burleigh was supported by the Office of Naval Research Parts of this research were performed while M. Burleigh held an NRC Research Associateship award at the NRL.

Data Availability Statement

Data (Burleigh, 2021) can be found at <https://rcweb.dartmouth.edu/LynchK/>. GEMINI is open-source software, kept and maintained in a public repository at <https://github.com/gemini3d/>.

References

- Amm, O., Aruliah, A., Buchert, S. C., Fujii, R., Gjerloev, J., Ieda, A., et al. (2008). Towards understanding the electrodynamics of the 3-dimensional high-latitude ionosphere: Present and future. In *Annales geophysicae: Atmospheres, hydrospheres and space sciences* (Vol. 26, pp. 3913–3932). Copernicus GmbH. <https://doi.org/10.5194/angeo-26-3913-2008>
- Arnoldy, R. L. (1977). The relationship between field-aligned current, carried by suprathermal electrons, and the auroral arc. *Geophysical Research Letters*, 4(10), 407–410. <https://doi.org/10.1029/GL004i010p00407>
- Brekke, A., Hall, C., & Hansen, T. (1989). Auroral ionospheric conductances during disturbed conditions. In *Annales geophysicae* (Vol. 7, pp. 269–280).
- Burleigh, M. (2021). *GEMINI simulation data for Isinglass study, repository “Dartmouth College Prof Kristina A Lynch”*. Retrieved from https://rcweb.dartmouth.edu/LynchK/pubdata/clayton_2021_jgr/data/
- Clayton, R., Lynch, K., Zettergren, M., Burleigh, M., Conde, M., Grubbs, G., et al. (2019). Two-dimensional maps of in situ ionospheric plasma flow data near auroral arcs using auroral imagery. *Journal of Geophysical Research: Space Physics*, 124(4). <https://doi.org/10.1029/2018JA026440>
- Dahlgren, H., Perry, G., St Maurice, J.-P., Sundberg, T., Hosokawa, K., Semeter, J. L., et al. (2014). 3D imaging reveals electrodynamics of polar cap aurora. *Astronomy and Geophysics*, 55(5), 526–528. <https://doi.org/10.1093/astroge/atu215>
- de la Beaujardiere, O., Vondrak, R., & Baron, M. (1977). Radar observations of electric fields and currents associated with auroral arcs. *Journal of Geophysical Research*, 82(32), 5051–5062. <https://doi.org/10.1029/ja082i032p05051>
- Doe, R. A., Vickrey, J. F., & Mendillo, M. (1995). Electrodynamical model for the formation of auroral ionospheric cavities. *Journal of Geophysical Research*, 100(A6), 9683–9696. <https://doi.org/10.1029/95ja00001>
- Donoho, D. L., & Duncan, M. R. (2000). *Digital curvelet transform: Strategy, implementation and experiment* (Department of Statistics, Stanford University Technical Report, Technical Report No 2000-12). Retrieved from <https://statistics.stanford.edu/research/digital-curvelet-transform-strategy-implementation-and-experiments>
- Fraunberger, M., Lynch, K. A., Clayton, R., Roberts, T. M., Hysell, D., Lessard, M., et al. (2020). Auroral ionospheric plasma flow extraction using subsonic retarding potential analyzers. *Review of Scientific Instruments*, 91, 094503. <https://doi.org/10.1063/1.5144498>
- Fujii, R., Amm, O., Yoshikawa, A., Ieda, A., & Vanhamäki, H. (2011). Reformulation and energy flow of the cowlung channel. *Journal of Geophysical Research*, 116(A2). <https://doi.org/10.1029/2010ja015989>
- Gillies, D. M., Knudsen, D. J., Donovan, E. F., Spanswick, E. L., Hansen, C., Keating, D., & Erion, S. (2014). A survey of quiet auroral arc orientation and the effects of the interplanetary magnetic field. *Journal of Geophysical Research: Space Physics*, 119(4), 2550–2562. <https://doi.org/10.1002/2013JA019469>
- Grubbs, G., Michell, R., Samara, M., Hampton, D., Hecht, J., Solomon, S., & Jahn, J.-M. (2018). A comparative study of spectral auroral intensity predictions from multiple electron transport models. *Journal of Geophysical Research: Space Physics*, 123(1), 993–1005. <https://doi.org/10.1002/2017ja025026>
- Grubbs, G., Michell, R., Samara, M., Hampton, D., & Jahn, J.-M. (2018). Predicting electron population characteristics in 2-D using multispectral ground-based imaging. *Geophysical Research Letters*, 45(1), 15–20. <https://doi.org/10.1002/2017gl075873>
- Heinselman, C. J., & Nicolls, M. J. (2008). A Bayesian approach to electric field and E-region neutral wind estimation with the Poker Flat Advanced Modular Incoherent Scatter Radar. *Radio Science*, 43(5). <https://doi.org/10.1029/2007rs003805>

- Hwang, K.-J., Lynch, K., Carlson, C., Bonnell, J., & Peria, W. (2006). Fast auroral snapshot observations of perpendicular DC electric field structures in downward current regions: Implications. *Journal of Geophysical Research*, *111*(A9). <https://doi.org/10.1029/2005ja011472>
- Kaeppler, S. R., Hampton, D. L., Nicolls, M. J., Strømme, A., Solomon, S. C., Hecht, J. H., & Conde, M. G. (2015). An investigation comparing ground-based techniques that quantify auroral electron flux and conductance. *Journal of Geophysical Research: Space Physics*, *120*(10), 9038–9056. <https://doi.org/10.1002/2015ja021396>
- Karlsson, T., Andersson, L., Gillies, D. M., Lynch, K., Marghitsu, O., Partamies, N., et al. (2020). Quiet, discrete auroral arcs—Observations. *Space Science Reviews*, *216*(1), 16. <https://doi.org/10.1007/s11214-020-0641-7>
- Karlsson, T., & Marklund, G. T. (1998). Simulations of small-scale auroral current closure ion the return current region. *Physics of Space Plasmas*, *15*, 401.
- Klatt, E., Kintner, P., Seyler, C., Liu, K., MacDonald, E., & Lynch, K. (2005). Sierra observations of Alfvénic processes in the topside auroral ionosphere. *Journal of Geophysical Research*, *110*(A10). <https://doi.org/10.1029/2004ja010883>
- Lynch, K., Hampton, D., Zettergren, M., Bekkeng, T., Conde, M., Fernandes, P., et al. (2015). Mica sounding rocket observations of conductivity-gradient-generated auroral ionospheric responses: Small-scale structure with large-scale drivers. *Journal of Geophysical Research: Space Physics*, *120*(11), 9661–9682. <https://doi.org/10.1002/2014ja020860>
- Mallinckrodt, A. J. (1985). A numerical simulation of auroral ionospheric electrodynamics. *Journal of Geophysical Research*, *90*(A1), 409–417. <https://doi.org/10.1029/ja090ia01p00409>
- Marghitsu, O. (2012). Auroral arc electrodynamics: Review and outlook. *Auroral Phenomenology and Magnetospheric Processes: Earth and Other Planets*, *197*, 143–158.
- Marghitsu, O., Karlsson, T., Klecker, B., Haerendel, G., & McFadden, J. (2009). Auroral arc and oval electrodynamics in the Harang region. *Journal of Geophysical Research*, *114*(A3). <https://doi.org/10.1029/2008ja013630>
- Marklund, G. (1984). Auroral arc classification scheme based on the observed arc-associated electric field pattern. *Planetary and Space Science*, *32*(2), 193–211. [https://doi.org/10.1016/0032-0633\(84\)90154-5](https://doi.org/10.1016/0032-0633(84)90154-5)
- Marklund, G., Sandahl, I., & Oppenorth, H. (1982). A study of the dynamics of a discrete auroral arc. *Planetary and Space Science*, *30*(2), 179–197. [https://doi.org/10.1016/0032-0633\(82\)90088-5](https://doi.org/10.1016/0032-0633(82)90088-5)
- Marklund, G. T., Ivchenko, N., Karlsson, T., Fazakerley, A., Dunlop, M., Lindqvist, P., et al. (2001). Temporal evolution of the electric field accelerating electrons away from the auroral ionosphere. *Nature*, *414*, 724–727. <https://doi.org/10.1038/414724a>
- Nicolls, M. J., Cosgrove, R., & Bahcivan, H. (2014). Estimating the vector electric field using monostatic, multi-beam incoherent scatter radar measurements. *Radio Science*, *49*, 1124–1139. <https://doi.org/10.1002/2014RS005519>
- Paschmann, G., Haaland, S., & Treumann, R. (2003). The aurora as a universal phenomenon. In *Auroral plasma physics* (pp. 415–434). Springer. https://doi.org/10.1007/978-94-007-1086-3_9
- Robinson, R., Vondrak, R., Miller, K., Dabbs, T., & Hardy, D. (1987). On calculating ionospheric conductances from the flux and energy of precipitating electrons. *Journal of Geophysical Research*, *92*(A3), 2565–2569. <https://doi.org/10.1029/ja092ia03p02565>
- Sugino, M., Fujii, R., Nozawa, S., Nagatsuma, T., Buchert, S. C., Gjerloev, J. W., & Kosch, M. J. (2002). Field-aligned currents and ionospheric parameters deduced from EISCAT radar measurements in the post-midnight sector. *Annales Geophysicae*, *20*(9), 1335–1348. <https://doi.org/10.5194/angeo-20-1335-2002>
- Zettergren, M., Lynch, K., Hampton, D., Nicolls, M., Wright, B., Conde, M., et al. (2014). Auroral ionospheric f region density cavity formation and evolution: Mica campaign results. *Journal of Geophysical Research: Space Physics*, *119*(4), 3162–3178. <https://doi.org/10.1002/2013ja019583>
- Zettergren, M., & Semeter, J. (2012). Ionospheric plasma transport and loss in auroral downward current regions. *Journal of Geophysical Research*, *117*(A6). <https://doi.org/10.1029/2012ja017637>
- Zettergren, M. D., Semeter, J. L., & Dahlgren, H. (2015). Dynamics of density cavities generated by frictional heating: Formation, distortion, and instability. *Geophysical Research Letters*, *42*(23), 10–120. <https://doi.org/10.1002/2015gl066806>
- Zettergren, M. D., & Snively, J. B. (2015). Ionospheric response to infrasonic-acoustic waves generated by natural hazard events. *Journal of Geophysical Research: Space Physics*, *120*(9), 8002–8024. <https://doi.org/10.1002/2015ja021116>
- Zettergren, M. D., & Snively, J. B. (2019). Latitude and longitude dependence of ionospheric TEC and magnetic perturbations from infrasonic-acoustic waves generated by strong seismic events. *Geophysical Research Letters*, *46*(3), 1132–1140. <https://doi.org/10.1029/2018GL081569>